Ion Implantation-Induced Plastic Phenomena in Metallic Alloys

Patrick H. Warren[1,2], Caleb D. Clement[1,3], Yongwen Sun[4], Jim Ciston[5], Colin Ophus[5], Yang Yang[4], Janelle P. Wharry[1*]

[1] School of Materials Engineering, Purdue University, West Lafayette, IN, USA 47907

[2] Department of Physics & Astronomy, University of Texas at San Antonio, San Antonio, TX, USA 78249

[3] Westinghouse Electric Company, LLC, Global Technology Development, Pittsburgh, PA, USA 15235

[4] Address

[5] National Center for Electron Microscopy Facility, Molecular Foundry, Lawrence Berkeley National Laboratory, Berkeley, CA, USA 94720

* Corresponding author (contact email: jwharry@purdue.edu)

ABSTRACT

Ion implantation is widely used for doping semiconductors or electroceramic materials and probing material behaviors in extreme radiation environments. But implanted ions can induce compressive stresses into the host material, which can induce plasticity and mesoscopic deformation. However, these phenomena have almost exclusively been observed in brittle ionic and/or covalently bonded materials. Here, we present transmission electron microscopy observations of unusual implantation-induced plasticity in two metallic alloys. First, Fe^{2+} ions induce dislocation plasticity below the implanted layer in a model Fe-P alloy. Next, He^{+} ions form pressurized cavities which activate the fcc-to-hcp strain-induced martensitic transformation in Alloy 625. In both cases, the plasticity can be explained by a combination of implanted ions being incorporated into the lattice and the creation of irradiation defects. These findings have significant implications for mechanical testing of ion implanted layers, while also opening pathways for using ion implantation to tune stress distributions in metallic alloys.

1. INTRODUCTION

Ion implantation is a widely used technique for doping semiconducting materials for enhanced electrical conductivity as microelectromechanical systems (MEMS) or microoptoelectromechanical systems (MOEMS) devices [1–3], doping electroceramic materials for improved performance in ion batteries [4–7], probing material performance in long-term space travel [8–11], and emulating the effects of neutron irradiation in nuclear fission and fusion reactor fuels and structural materials [12,13]. But ion implantation is well known to introduce compressive stresses into the host materials through two major mechanisms: (1) accommodation of implanted ions into the host lattice [14], and (2) creation of irradiation damage if the incident ion energies are sufficiently high – i.e., a supersaturation of vacancies and interstitials, and their coalescence into extended defects such as dislocation loops and cavities [15–18]. In the former mechanism, lattice expansion occurs as implanted ions become incorporated into the lattice; this lattice expansion is sensitive to crystallographic orientation [19–21] but is typically constrained by the unirradiated substrate, resulting in a biaxial compressive stress [17]. Similarly, in the latter mechanism, compressive stresses are generated by volumetric expansion associated with extended irradiation defects.

The majority of studies on ion implantation-induced stresses and their implications, have been performed on ionically and/or covalently bonded materials, including Si and silicates [16], sapphire [22], Al_2O_3 [17,18], and Synroc B, a ceramic composite intended for radioactive waste immobilization [23], or in glassy materials [24,25]. In these materials that classically exhibit brittle mechanical behaviors, the compressive stresses generated by ion implantation can lead to plastic deformation [26,27] and may result in changes to hardness, flexural strength, fracture toughness, and wear resistance [18]. These induced stresses are sensitive to the implantation

temperature and ion specie [17,18], and generally increase with irradiation dose until a steady-state stress level is reached. The implantation-induced residual compressive stress exhibits a Gaussian depth profile, in which the position of the maximum stress and the area of the distribution are also dependent on the ion energy and specie [14].

In these relatively brittle materials, ion implantation-induced stresses in thin films and nanostructured materials often manifest mesoscopically as bending deflection [16,28]. For example, Arora, et al. [29] shows that 30 keV Ga^+ ion implantation on 190 nm thick amorphous Si_3N_4 cantilevers causes significant stress gradients that fold the cantilever at the irradiated region. Chalifoux, et al. [30] use ion implantation to intentionally introduce stresses that counteract intrinsic stresses retained during the deposition of reflective Cr coatings on Si wafers that result in intrinsic deflections ranging 400-1600 nm. They show that 2 MeV Si^{2+} ions are capable of returning the coated wafers to negligible deflections ≤60 nm. A similar study from Bifano, et al. [31] also demonstrates that Ar ion machining-induced compressive stresses can be used to counteract pre-existing curvature in pure Si wafers.

Two other factors that influence stress distributions are sputtering and order-disorder transformations. Particularly in semiconductors and ceramics, stresses generated during ion implantation can at least partially be attributed to irradiation-induced crystalline-to-amorphous [16,22,31,32] or amorphous-to-crystalline transformations [28,33]. During these transformations, the differences in interatomic spacing and atomic volume between the crystalline and amorphous phases inherently gives rise to internal stresses and causes bending [28,32]. Sputtering, which refers to the erosion of surface atoms from the target material due to the incident ion beam, can also affect the resultant stress distribution in the target [29,31]. While implantation-induced stresses are generally compressive, sputtering introduces tensile stresses that can be sufficiently

large as to alter the direction of the mesoscopic bending deflection in the amorphous Si_3N_4 thin film cantilevers [29].

In metallic materials having high plasticity and/or low yield strength, only limited studies have reported ion implantation- or irradiation-induced stresses. The majority of these reports have observed "long-range effects", a phenomenon in which defect structures form in an ion irradiated and implanted material at depths more than an order of magnitude greater than the projected ion range [34–37]. Long-range effects are often associated with changes to physical and mechanical properties of the material, such as increasing hardness and wear resistance and are thought to be caused by static and dynamic stresses as well as acoustic and elastic waves [34]. Sharkeev and coworkers [34] have summarized reports in the literature of long-range effects and have classified these effects into two categories: (1) formation of dislocation loops, pores, or point defects at unexpectedly deep distances below the ion implantation profile, and (2) formation of dislocation structures below the ion implantation profile. The mechanisms responsible for these classes of long-range effects are not well understood and have not been systematically researched. But in a follow-on study, Sharkeev proposes that the dislocation structures form when ion implantation induces stresses exceeding the yield strength of the material, causing dislocation emission from the implantation zone at sufficiently high velocities such that inertia carries them deeper into the unirradiated substrate [35]. The extent of long-range effects depend on the magnitude and sign (compressive or tensile) of residual stress in the target material [35].

Even fewer reports have observed short-range (i.e., within or adjacent to the implantation region) stress effects due to ion implantation or irradiation in metallic materials. But these few studies highlight the importance of pores or cavities in stress generation. One study from Misra,

et al. [38] uses 33-330 keV C, Xe, or Ar ion implantation of Cr films having varied residual stresses ranging from tensile to compressive. Films with large tensile residual stresses develop implantation-induced columnar porosity, and the internal stresses reach a tensile maximum before reverting to a compressive stress and tending toward a steady-state. Meanwhile the films with compressive residual stress develop a dense, non-porous implantation microstructure and tend toward a steady-state compressive stress. These behaviors can be explained by the decreasing interatomic distances with increasing irradiation dose [39], potentially due to defect clustering [40]. In another study, Dahmen, et al. [41] intentionally induce sputtering of (100)-oriented Cu crystals using 800-2200 V noble gas ions (Ar, Ne, and He), and measure compressive stresses on the order of 2-15 N/m. They find that the magnitude of stress and the time to stress saturation are dependent on the ion energy and specie, and are governed by a competition between sputtering-induced material removal and the outward pressure of the implanted gas ions and the extended gas bubbles they form.

While the literature has shown that ion implantation and gas bubbles play a role in generating stresses, there remains a lack of unifying theory or understanding of stress effects from ion implantation/irradiation in crystalline metallic alloys. The existence of short-range effects of ion implantation/irradiation in metals is itself not a widely acknowledged phenomenon. In the present study, two case studies are considered which provide evidence of short-range stress effects in metallic alloys. In the first case, self-ion irradiation forms an irradiation damage and implantation layer, and subsequently generates dislocation plasticity in the unirradiated substrate. In the second case, noble gas ion implantation is conducted to introduce cavity defects in the implantation zone, which induce localized plasticity. Potential mechanisms of these plastic behaviors are discussed. These findings shed light on a possible phenomenon that may have

significant consequences for future studies that aim to use ion implantation and irradiation to evaluate microstructure evolution and mechanical property changes in metallic alloys. This work also creates opportunities to use ion irradiation to tune properties of metallic alloys in the same manner as can be done in ceramic materials.

2. METHODS

2.1 Materials & Irradiations

This work focused on two alloys, a supersaturated Fe-2.55P (in wt%) binary model alloy and the commercial Ni-based Alloy 625, with compositions provided in **Table 1**. The binary alloy was fabricated as a button using vacuum arc melting at Ames Laboratory, as described more comprehensively in [42]. The Alloy 625 was forged in an ingot form and furnished by the Electric Power Research Institute (EPRI). It was hot rolled and solution annealed, followed by a two-step heat treatment that was not intended to induce γ' or γ" precipitation; comprehensive processing details can be found in [43]. It is also worth noting that this identical forging of Alloy 625 was included in an extensive neutron irradiation campaign [44–46] and its grain-level stress distributions were shown to be homogeneous through synchrotron X-ray high energy diffraction microscopy (HEDM) with *in situ* straining [47]. Both alloys were cut into matchstick specimens using electrical discharge machining (EDM); matchstick dimensions were 1.5 x 1.5 x 20 mm for the Fe-P alloy, and 2 x 4 x 20 mm for Alloy 625. The matchstick surface was ground using SiC paper, working up through 1600 grit, then sequentially polished in a diamond slurry of 6, 3, and 1 μm particle sizes. The specimens were then vibratory polished in 0.5 μm silica slurry for 4 hours. Finally, specimens were electropolished using a Buehler ElectroMet 4 operating at 25 V

for 15 sec with a Pt mesh cathode in a 10% perchloric acid and 90% methanol solution held at -40°C.

The Fe-P specimen was irradiated with 4.4 MeV Fe^{2+} ions at a temperature of 370 ± 5°C. The Stopping Range of Ions in Matter (SRIM) 2013 software [48] was run in Quick Kinchin-Pease mode [49] to calculate the damage and ion implantation profiles, **Figure 1(a)**. The total ion fluence was 1.66 x 10^{16} ions/cm^2, which corresponds to a total damage dose of 8.5 dpa at a depth range of 400-600 nm, for a dose rate of 7.6 x 10^{-4} dpa/sec. The Alloy 625 specimen was irradiated with He ions at 500 ± 5ºC. To achieve an approximately uniform He implantation layer, multiple He energies were used, ranging 200-800 keV. Individual damage profiles for each ion energy were calculated with SRIM using the Quick Kinchin-Pease mode, and were then aggregated into a cumulative implantation profile, **Figure 1(b)**. The relatively uniform He implanted region extended over 500-1500 nm and had a nominal cumulative implantation fluence of 6.5x10^{15} ions/cm^2. All irradiations were conducted at the Michigan Ion Beam Laboratory using the Wolverine 3 MV tandem particle accelerator (Fe and He >400 keV) and Blue 400 kV ion implanter (He <400 keV).

2.2 Characterization

For Fe-P, grain orientations on the irradiated surface were mapped using scanning electron microscopy (SEM) with electron backscatter diffraction (EBSD), and neighboring grain pairs oriented near (001) and (011) were identified. A TEM lamella was extracted from across the identified grain boundary using the FIB lift-out technique. The resultant lamella was a (001)/(011) bicrystal and contained a cross-section of the irradiation damage and ion implantation profiles. The TEM lamella was welded to a Cu half-grid, then thinned to electron

transparency of ~80 nm, following procedures as described in [42]. For the irradiated Alloy 625 specimen, a cross-sectional TEM lamella was extracted from a random grain, then prepared following similar procedures as for the Fe-P lamellae. The Fe-P work was conducted in an FEI (now Thermo Fisher Scientific) Quanta 3D FEG dual-beam SEM/focused ion beam (FIB) at the Microscopy and Characterization Suite (MaCS) at the Center for Advanced Energy Studies (CAES), and the Alloy 625 work was conducted on a Thermo Fisher Scientific Helios G4 UX dual-beam SEM/FIB at Purdue University.

TEM characterization of the Fe-P specimen was carried out by tilting each grain to the nearest zone axes, which were [111] and [113] for the (011) and (001) grains, respectively. Selected area electron diffraction (SAED) patterns were collected from both the ion implanted region and the unirradiated substrate to measure the effect of irradiation on the lattice parameter. The microstructures of the irradiated region and unirradiated substrate were imaged using bright field scanning TEM (BF-STEM). All TEM/STEM characterization of the Fe-P lamellae was conducted in the FEI Tecnai TF30-FEG STwin TEM in the MaCS Laboratory at CAES. For the Alloy 625, helium implantation-induced cavities are imaged using the Fresnel through-focus technique. A combination of electron diffraction pattern analysis, high-resolution TEM (HR-TEM), and high-resolution scanning TEM (HR-STEM) were used to confirm phases present and the atomic stacking sequences. At high-resolution, Fast Fourier Transformations (FFT) were used as a surrogate for diffraction patterns to examine nanoscale areas for evidence of secondary phase formation [50]. Energy dispersive X-Ray spectroscopy (EDS) was conducted using a SuperX EDS detector to evaluate chemical homogeneity. All TEM/STEM characterization of Alloy 625 was conducted using a Thermo Scientific Themis Z at Purdue University. In addition, 4D STEM strain mapping was conducted on the He implanted Alloy 625 specimen using the

double-aberration-corrected TEAM 1 microscope at the National Center for Electron Microscopy (NCEM) at Lawrence Berkeley National Laboratory. The instrument was operated at 300 keV with 0.9 mrad convergence semi angle, 2 Å step size, and 630 mm camera length. Diffraction data was collected using a Gatan K3-IS electron counting detector located behind a Gatan Continuum imaging filter. All diffraction data was collected with an energy slit around the zero-loss peak to suppress diffuse background from plasmon and other inelastic losses. A 20 micron bullseye probe-forming aperture was used for high-precision identification of peak positions [51], and py4DSTEM software was used for data analysis [52].

3. RESULTS

The Fe-P bicrystalline lamella has a ~1.3 μm damage and implantation layer below the surface, **Figure 2(a)**. The irradiation damage layer is distinguished by a high density of darkly-contrasting defects in BF-STEM imaging, while the ion implantation region is a dark-contrasting band located ~0.9-1.3 μm below the surface that correlates favorably with the predicted SRIM damage and implantation profiles. The irradiated region of the (011) grain has a higher defect density than the (001) grain, **Figure 2(b-c)**, although this manuscript does not focus on quantifying irradiation defects; complete characterization of the irradiation defects is provided in ref. [42]. Below the irradiated and implanted layer is a layer of linear dislocation-type defects in the unirradiated substrate of both the (001) and (011) grains, which may be either dislocation lines or Frank loops. Note the material is defect-free under similar imaging conditions before irradiation, **Figure 2(d)**. The induced substrate dislocation-type features appear longer and are present a higher linear density in the (011) grain than in the (001) grain. In addition, the dislocation-type plasticity in the (011) substrate extends deeper than in the (001) grain. In the

(011) grain, the dislocation density over a depth range ~1.3-1.8 μm is 20.8 μm^{-2}, then decreases to 5.9 μm^{-2} over a depth range ~1.8-3.7 μm. By contrast, in the (001) grain, the dislocation density over a depth range ~1.3-1.6 μm is only 8.5 μm^{-2}; the grain is dislocation-free below ~1.6 μm. Lattice parameters, determined by measuring *d*-spacing from SAED patterns inset in **Figure 2(b-c)**, in the ion implanted region of the (001) and (011) grains are 0.303 nm and 0.304 nm, respectively. Meanwhile, the unirradiated lattice parameter is 0.291 nm [42] as measured in the same Fe-P material and reported in a previous study.

In the He ion implanted Alloy 625, BF-STEM imaging down the [101] zone axis reveals a band of implantation-induced defects at a depth ranging 0.5-1.5 μm, **Figure 3**. The inset diffraction pattern in **Figure 3(a)** indicates the possible presence of hcp martensite in the implantation region, while **Figure 3(b)** points out the He bubbles both existing freely in the microstructure and decorating the martensite features. The average He bubble radius is 3.48 ± 0.06 nm and their number density within the implanted region is 3.48 ± 1.63 $x10^{21}$ m^{-3}. A combination of HR-TEM and diffraction of the martensite-like features in **Figure 4** confirms these overlapping bundles of stacking faults on successive <111> planes form a secondary hcp ε-martensite phase. Diffraction shows two clear lattices, one belonging to the parent γ-fcc phase, and the other belonging to the secondary ε-hcp phase, following the distorted Shoji-Nishiyama orientation relationship (OR) previously reported for deformation-induced martensite in Alloy 625 as [53]:

$$(111)_\gamma // (01\bar{1}\bar{2})_\varepsilon\,,\ [110]_\gamma // [\bar{2}3\bar{2}4]_\varepsilon$$

These multilayered banded deformation structures likely include a combination of faulted ε-martensite, deformation twinning, and parent γ-fcc; high levels of strain amongst these features can explain the distorted OR. Streaks in the diffraction pattern along the {111} direction are indicative of planar features such as bundles of stacking faults (i.e., ε-martensite) [54].

Since strain-induced martensitic transformations are not conventionally believed possible in high-stacking fault energy (SFE) alloys such as Alloy 625, one can consider the possibility that these features are simply faulted loops. While faulted loops can provide similar diffraction pattern streaks as shown in **Figure 4(a)** inset [55], loops are only a single atomic plane as compared to the multiple atomic-layer features herein. Additionally, close examination of the atomic structure at the features of interest, **Figure 4(b-c)**, reveals a stacking fault on the atomic planes, which is characteristic of an ε-martensite feature, whereas dislocation loops are coherent with the surrounding atoms. Additionally, in **Figure 5**, EDS mapping indicates there is no chemical segregation to the hcp martensites or the He bubbles which preferentially decorate them, confirming that these features are diffusionless or strain-induced. Moreover, these EDS results also rule out the possibility that these features are not likely irradiation-induced, as they are free of radiation-induced segregation.

Additionally, 4D STEM strain mapping confirms the mechanical nature of these features. A high angle annular dark field (HAADF) image of two intersecting planar martensite features, indicated with a dashed line, with He bubbles arrowed, is shown in **Figure 6(a)**. The resultant maps of principal strains (ε_{xx}, ε_{yy}), **Figure 6(b)**, reveal that atomic planes are in compression (blue) around the planar martensite feature and the bubbles, while the regions further away from these features are in tension (red); there is little shear (ε_{xy}) strain from these features. Note that strains are not absolute strains, but are relative strains within a single map. Additionally, grain rotation (Θ) occurs between the two intersecting planar martensites, toward the left of the image. While a faulted loop would likely create similar compressive strains in the surrounding atomic planes, the grain rotation cannot be caused by faulted loops, but must be caused by a mechanical shearing effect from the intersection of the mechanical martensites. Moreover, **Figure 6(c)** shows the [110] zone axis diffraction pattern of the red boxed region from **Figure 6(a)**,

revealing streaks along the {111} direction. In FCC materials, planar defects such as stacking faults or twins generate streaks along this exact direction on this exact zone axis [56].

Finally, recent work from Clement, et al. [53] has revealed the existence of fcc-hcp transformations in Alloy 625 due to dislocation pinning at oversized solute atoms that hinder stress relaxation through conventional dislocation plasticity. Clement's work theorized that high strain or high strain rates are necessary for inducing martensitic transformations, though the present observations suggest these transformations may be even easier to initiate. Note that sputtering is not expected to play a significant role in the present results, since sputtering is highly sensitive to crystallographic orientation and the sputtering yield is expected to be low, ~1 nm for the ion energies herein [57].

4. DISCUSSION

4.1 Irradiation/Implantation Strain in Fe-P and Other Competing Explanations

Studies have established that the buildup of implanted ions and point defects results in an increase in the lattice parameter of the target material [19,58–60]. But the presence of dislocations in the unirradiated substrate – which are not present before irradiation – implies that this lattice expansion is associated with sufficient residual stress that plastic strain may be induced. Based on the ion fluence (1.66×10^{16} ions/cm^2) in the current study, a total of 2.49×10^{15} Fe^{2+} ions become implanted in a volume of 1.95×10^{16} nm^3 (i.e., a 1.5 mm x 10 mm irradiation area x 1.3 μm implantation depth). If this volume is allowed to expand and this expansion is confined to the thickness dimension (i.e., implantation direction), the resultant lattice parameter expansion would be 0.018 nm, or ~6%. However, the actual measured lattice expansion is ~0.012-0.013 nm, representing ~4% expansion (Section 3). This difference in lattice

expansion could be explained by relaxation of some stresses on the free surface. Irradiation-induced stress relaxation at free surfaces has been shown to occur in metallic alloys through modification of the dislocation structure [61,62] and through viscous flow, a creep-like mechanism [63].

Carrying the implanted ion calculation further, the calculated volume expansion would generate a strain on the substrate of 7.88×10^{-7} (note an equivalent strain is assumed to be lost to the free surface). This strain is comparable to the compressive strains calculated for other ion implantations in microelectronic materials, when scaling for the total ion fluence [29,31,41,64]. But assuming an elastic modulus for bcc Fe of 213 GPa, the resultant stress on the substrate would be only 0.17 MPa, which is well below the yield stress. However, if the volume expansion also considers irradiation-induced self-interstitials (calculated by SRIM), the strain on the substrate would increase to 4.00×10^{-3} which corresponds to a stress of 851 MPa. This value is likely an overestimate, since SRIM simulations tend to overestimate the amount of implanted ions that get incorporated into the target lattice [65]. Thus, the actual stress applied to the substrate is likely close to the 631 MPa compressive residual stress measured in a stainless steel plate irradiated to similar conditions as the current study (3 MeV Fe^{2+} ions to a fluence of 3×10^{16} ions/cm^2, measured using depth-sensing nanoindentation by Wang, et al. [66]). Obviously, these simple calculations in the present study ignore factors such as point defect recombination and the formation of extended defects. Nevertheless, these simple stress calculations concur with conclusions from Misra, et al. [38], suggesting that ion implantation alone is likely insufficient to induce plasticity in the substrate, but that the combination of implantation and the production of irradiation-induced defects may generate stresses sufficient to induce substrate plasticity.

In the (011) grain, the longer dislocations, higher linear density, and persistence of dislocations deeper into the substrate imply a higher strain in that grain than in the (001) grain. This is likely because the (011) plane serves as the primary slip plane in bcc Fe, so critical resolved shear stress (CRSS) may be higher on the active slip system(s) in the (011) oriented grain. However, determination of dislocation type, habit plane, and CRSS across the two grains is beyond the scope of this study. In addition, the higher atomic planar density in the (011) grain, 17.17 nm^{-2}, compared to that of the (001) grain, 12.14 nm^{-2}, could also lead to greater production of irradiation-induced self-interstitial atoms in the (011) grain. That is, the higher atomic planar density will increase the probability of ion-atom collisions, thus generating more displacements and creating more self-interstitial atoms in the (011) grain; this is corroborated by the higher defect density in the irradiated region of the (011) grain than in the (001) grain. This larger population of defects can generate greater residual stress in the substrate. The crystallographic orientation dependence of the accumulation, morphology, and penetration depth of irradiation-induced defects has been attributed differences in atomic planar density in an fcc Ni-based alloy [67] and in pure W [68].

The existence of a dislocation microstructure below – but associated with – the irradiated layer in the Fe-P alloy is similar to the concept of the long-range effects of ion implantation studied by Sharkeev and coworkers [34,37]. However, true long-range effects are generally observed ~10s of μm below the implantation zone (which can be as shallow as a few ~10s of nm) [37], whereas the dislocations in the present study are confined to <2 μm below the implantation zone. It is worth noting that these depths of long-range effects are not directly correlated to the irradiating ion energy. In addition, ion implantation long-range effect dislocations in ductile bcc metals such as Mo and α-Fe tend to be kinked, cross-slipped, and

form subgrain-like structures [34,35]. By contrast, the dislocations in the Fe-P alloy are linear, with few kinks and limited cross-slip. Subgrain structuring becomes even more characteristic of ion implantation long-range effects in harder materials such as TiN ceramic, in which grain boundaries act as stress concentrators that can emit dislocations to relax stresses [36]. An oscillatory stress field is generated along the interface between the implantation zone and the substrate; dislocation emission and subgrain formation compete to relax these stresses, causing dislocations to penetrate into the substrate if the initial grain size is sufficiently refined [36]. Lacking evidence of subgrain structuring, let alone dislocation kinking or cross-slip, long-range effects are not likely responsible for the Fe-P substrate plasticity observed in the present study.

A competing theory from Lu, et al. [69] suggests that defects can be found beyond the projected ion implantation range due to defect migration during prolonged irradiation. In their study of single crystal Ni, Ni-50Co, and Ni-50Fe irradiated with 3 MeV Au ions to a fluence of 2 x 10^{13} ions/cm^2, corresponding to a peak dose of 0.12 dpa, they observe dislocation loops and stacking fault tetrahedra (SFT) in the unirradiated, unimplanted substrate. These extended defects are thought to form in the substrate due to point defect and defect cluster migration during irradiation, given the relatively low migration barriers of 0.3-0.4 eV for vacancy clusters and 0.8 eV for vacancy clusters having an SFT-like structure [69]. However, this explanation does not reconcile the sub-implantation microstructure in Fe-P, which is comprised exclusively of dislocations and is absent of irradiation-like extended defects such as loops or SFTs.

4.2 Role of Irradiation/Implantation Cavities in Strain-Induced Transformations

Building upon the observation in Fe-P that the combination of implantation and the production of irradiation-induced defects may generate stresses exceeding plastic yield, we

consider the role of extended defects – specifically, cavities – in initiating strain-induced phase transformations. Cavities can include vacuum-filled voids as well as gas-pressurized bubbles, which can be difficult to distinguish, especially when they are too small to resolve crystallographic faceting by TEM [70–73]. Often, both irradiation-induced vacancies and gas ions coalesce to form partially pressurized bubbles [74], which create compressive stresses on the surrounding material and can lead to mechanical degradation [75,76]. These stresses can be estimated by considering the associated volumetric swelling [77] using the following form assuming a narrow cavity size and density distribution:

$$\varepsilon = \frac{4}{3}\pi \bar{R}^3 \rho_v \quad (1)$$

where $\bar{R}$ is the average cavity radius and ρ_v is their number density. For the He implanted microstructure characterized herein, the calculated swelling is 0.062%. This can be related to the hydrostatic stress induced in the system using the following form [78]:

$$\sigma = \frac{E}{1-2\nu}\varepsilon \quad (2)$$

Where E is the elastic modulus (207.5 GPa) and ν is the Poisson's ratio (0.278).

For a gas-filled bubble to maintain equilibrium, i.e., outward-acting gas pressure in equilibrium with the inward-acting surface energy, the change in free energy of the solid takes the following form [74]:

$$dG = Vdp + \gamma dA \quad (3)$$

$$Vdp = d(pV) - pdV \quad (4)$$

Assuming an ideal gas, pV is constant and V=4/3πR^3, resulting in the form:

$$\frac{dG}{dr} = -4\pi R^2 (p - \frac{2\gamma}{R}) \quad (5)$$

Where γ is the surface energy (2.34 J/m^2 for Ni [79]). With dG/dr = 0 to maintain equilibrium, the pressure of the gas-filled bubble in the presence of stress is:

$$p = \frac{2\gamma}{R} - \sigma \quad (6)$$

From Equations 1-6 the pressure of a gas-filled bubble in this study is calculated to be 1344 MPa. Alternatively, if the cavity is not subject to mechanical equilibrium, its pressure can be calculated from the ideal gas law assuming:

$$p = \frac{3nkT}{4\pi\bar{R}^3} \quad (7)$$

Where n is the number of gas atoms per cavity, k is the Boltzmann constant, and T is the temperature. Given the known irradiation fluence and average bubble radius, the pressure is calculated to be 1129 MPa.

Both of these calculated stresses exceed the nominal yield stress of this same material reported in [78], although the incorporation of irradiation-induced vacancies in the cavities would reduce these calculated stresses. Nonetheless, it is possible that an accumulation of He-pressurized cavities may create sufficient internal strain and accompanying stress to initiate martensitic transformations. Even without internal gas pressure, Mao, et al. [72,80–82] have shown that the energy of the internal surface created by the formation of cavities, can contribute toward offsetting or reducing the critical stress required to initiate martensitic transformations in 304L austenitic stainless steel at room temperature (M_{d30} ~20-40ºC, i.e., temperature at which 50 vol% of α'-martensite forms at 30% strain [83]). Molecular dynamics simulations have also confirmed the role of non-pressurized voids in fcc alloys in concentrating stress and enabling martensitic transformations in a concentrated Fe-50%Ni alloy at 300K [84]. Here, then, the combination of cavity surface energies and internal gas pressure, may act synergistically to activate martensitic transformations. That being said, it may also be plausible that early cavity-

induced martensitic transformations subsequently act as preferential nucleation sites for additional cavities.

The residual stress associated with a He-implanted surface has been quantified by Hosemann, et al. [85] for the case of He blistering. But whereas the He blister has only a ~few nm of metallic material between the blister and the free surface, the He implanted region in the present study is located ~500 nm from the free surface. Previous studies with self-ion implanted tungsten show that ion implantation-induced strain is limited to the implantation region [86]. It is therefore postulated that the unimplanted region at depths 0-500 nm serves as a quasi-immovable boundary that may limit swelling and maximize pressure within the implanted region. Hence, we treat the cavities as fully constrained and spherical, as opposed to He blisters which grow in essentially one direction by virtue of proximity to a free surface.

It is also worth contrasting that stress introduced by He implantation is relieved within the implanted layer, whereas stress introduced by Fe implantation is relieved in the substrate below the implanted layer. This difference may partially be due to the gas pressure of He cavities, which exert stress somewhat consistently throughout the implanted layer where these cavities are present, owing to the variable He ion energies used. On the other hand, in the Fe irradiated material, we previously state that plasticity is likely caused by irradiation-induced point defects as well as implanted Fe ions. The peak concentrations of these defects and Fe interstitials fall within the depth range ~1000-1500 nm due to the monoenergetic nature of the ions. But since the material at depths <1000 nm is irradiation hardened and more resistant to dislocation plasticity, stress may be more easily relieved by inducing plasticity in the softer substrate.

4.3 Implications of the Present Findings

While the role of ion implantation and irradiation on generating stress in metallic alloys is not surprising, there has previously been little microstructural evidence of such significant short-range irradiation- or implantation-induced plasticity. The present results add further complexity to the already challenging problem of studying the microstructural evolution and mechanical behavior of ion irradiated near-surface layers. In particular, the mechanical behavior of ion irradiated layers has been probed by numerous micro-scale methods, such as nanoindentation [87–96], micro-compression pillars [97,98], and micro-tensile bars [99,100], often through SEM *in situ* [101–104] and TEM *in situ* [105–113] configurations. These micro-/nano-scale loading configurations pose challenges of localizing plastic zones and limiting our ability to extract meaningful quantitative mechanical properties, in part due to strength and stiffness differences between the irradiated layer and the unirradiated substrate, i.e., the "soft substrate" effect [95,105,114–117]. The present findings imply that implantation/irradiation-induced strain hardening in both the irradiated layer and the substrate must be considered when interpreting small-scale mechanical testing data and selecting material properties for finite element analysis models used to aid in data analysis. In addition, TEM microstructure characterization *post mortem* to deformation of ion irradiated materials must be interpreted carefully to appropriately decouple the effects of deformation from irradiation.

5. CONCLUSIONS

The development of stress associated with ion implantation and irradiation has been studied in two metallic alloys: a model Fe-2.55P (in wt%) alloy irradiated with 4.4 MeV Fe^{2+} ions at 370°C, and a commercial Ni-based Alloy 625 implanted with He^{+} ions of multiple

energies. Cross-sectional TEM characterization of both specimens reveals unusual ion implantation- and/or irradiation-induced plastic strain effects. In the Fe-P, dislocation plasticity occurs in the unirradiated substrate, immediately below the ion implantation zone. The extent of this plasticity is greater in an (011) oriented grain than in a (001) oriented grain, due to the critical resolved shear stress together with the effects of atomic planar density on the development of irradiation defects. In the Alloy 625, the fcc-to-hcp strain-induced martensitic transformation is associated with cavities from ion implantation. In both alloys studied, ion implantation and the irradiation-induced defects (point defects and extended defects), act synergistically to introduce sufficient stress in the material so as to cause plastic deformation. The location of the plastic deformation (whether in the irradiated layer or in the substrate) is dependent on the nature of the defects responsible for stress buildup. These findings have significant implications on the evaluation of mechanical properties of ion implanted or ion irradiated materials, but also present the possibility of using ion irradiation or implantation to tune nanoscale mechanical responses of metallic alloys.

ACKNOWLEDGEMENTS

The authors thank Dr. Yaqiao Wu, Dr. Yu Lu, Megha Dubey, Jeremy Burgener, and the staff at CAES for their assistance with microscopy, specimen handling, and work coordination, and Dr. Rosa Diaz and Dr. Zhongxia Shang at Purdue University for assistance with microscopy. This work was partially supported by the National Science Foundation award DMR-17-52636 and partially supported by the U.S. Department of Energy, Office of Science, Basic Energy Sciences, under award DE-SC0020150. P.H.W. and C.D.C. also acknowledge fellowship support from the United States Nuclear Regulatory Commission under grant 31310021M0035. Alloy 625 He

implantation experiments and characterization were supported by the US Department of Energy, Office of Nuclear Energy, through the Nuclear Science User Facilities (NSUF) experiment award 22-4415. 4D STEM strain mapping work at the Molecular Foundry was supported by the Office of Science, Office of Basic Energy Sciences, of the U.S. Department of Energy under Contract No. DE-AC02-05CH11231.

DATA AVAILABILITY

Data will be made available upon request.

DECLARATION OF COMPETING INTERESTS

On behalf of all authors, the corresponding authors states that there is no conflict of interest.

CRediT AUTHORSHIP CONTRIBUTION STATEMENT

Jim Ciston: Investigation, Writing- review & editing. **Caleb D. Clement:** Conceptualization, Funding Acquisition, Investigation, Formal Analysis, Writing- original draft, Writing- review & editing. **Colin Ophus:** Investigation, Writing- review & editing. **Yongwen Sun:** Formal Analysis, Writing- review & editing. **Patrick Warren:** Conceptualization, Investigation, Data Curation, Formal Analysis, Writing- original draft. **Janelle P. Wharry:** Conceptualization, Funding Acquisition, Writing- original draft, Writing- review & editing. **Yang Yang:** Formal Analysis, Writing- review & editing.

TABLES & FIGURES

Table 1: Chemical compositions (wt%) of alloys investigated.

Alloy	Ni	Cr	Mo	Fe	Nb	Ti	Al	Si	Mn	P	S	C
Fe-P	–	–	–	Bal.	–	–	–	–	–	2.55	–	–
625	Bal.	23.7	7.58	3.52	3.57	0.31	0.31	0.20	0.42	0.006	0.004	0.01

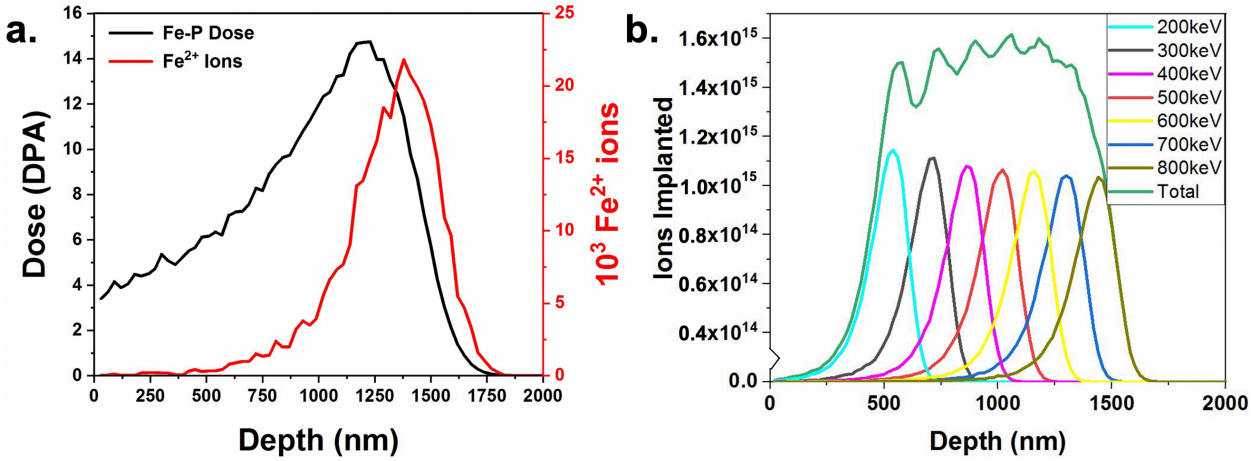

Figure 1: (a) SRIM damage and implantation profiles for 4.4 MeV Fe ions incident on Fe-P alloy; and (b) aggregated SRIM damage profiles and cumulative He implantation for variable-energy He ion irradiation of Alloy 625.

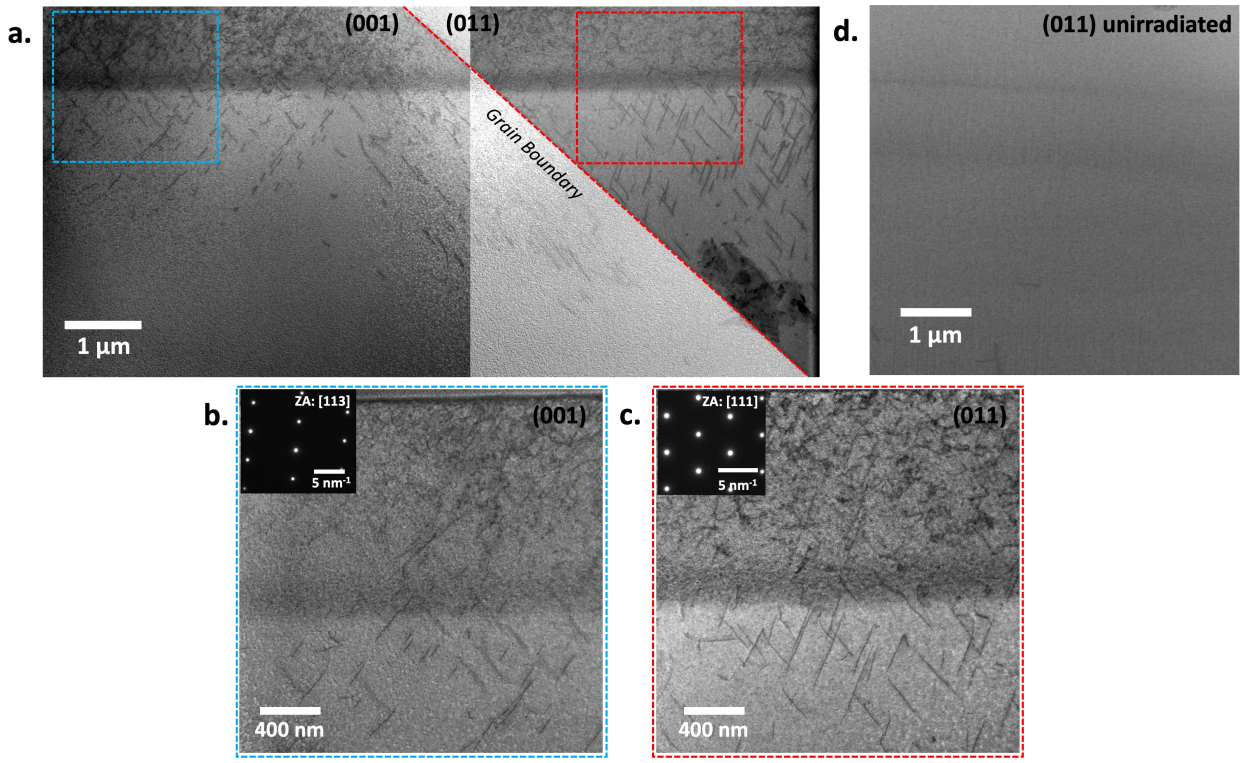

Figure 2: (a) Stitched composite micrograph of (001)/(011) bicrystalline Fe-P lamella grain (left) and (011) grain (right) with grain boundary indicated in red; higher magnification images of (b) (001) irradiated region with unirradiated substrate and (c) (011) irradiated region with unirradiated substrate, showing substrate dislocations; (d) (011) unirradiated Fe-P microstructure is free of dislocations.

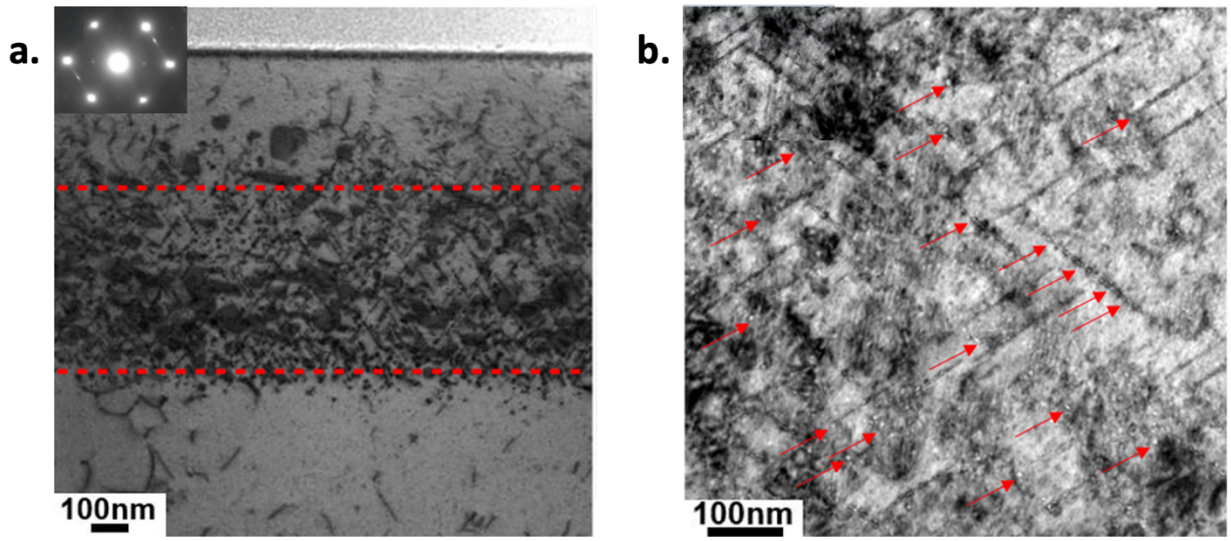

Figure 3: (a) Representative micrograph of He implanted Alloy 625 with dashed lines detailing the 500-1500 nm implantation region, and (b) BFTEM underfocused micrograph with arrows indicating He bubbles in the microstructure.

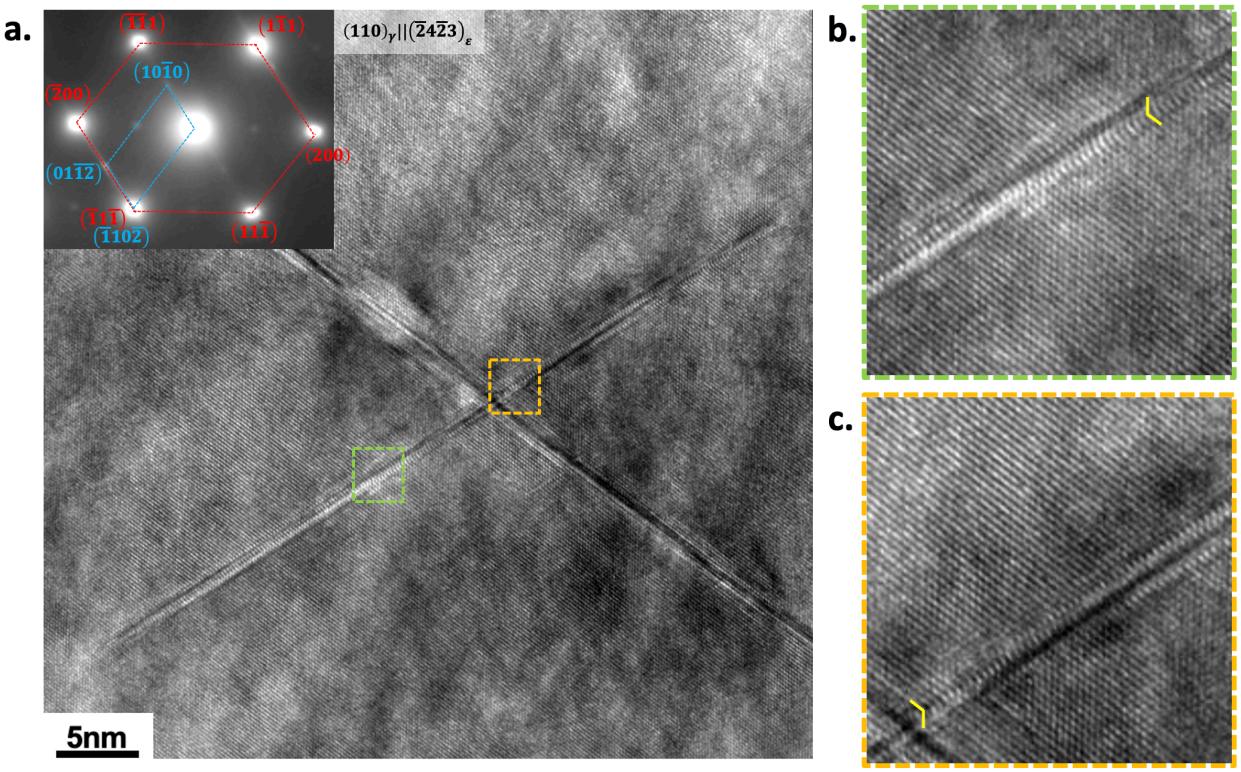

Figure 4: (a) HRTEM micrograph of bubble-decorated intersecting hcp martensites in He implanted Alloy 625 taken along [110] zone axis, with FFT inset showing indexing describing the distorted fcc-hcp Shoji-Nishiyama orientation relationship; boxed regions are correspondingly shown at higher resolution in (b) and (c) to reveal the stacking fault (marked with yellow arrow) of atoms characteristic of martensite structure.

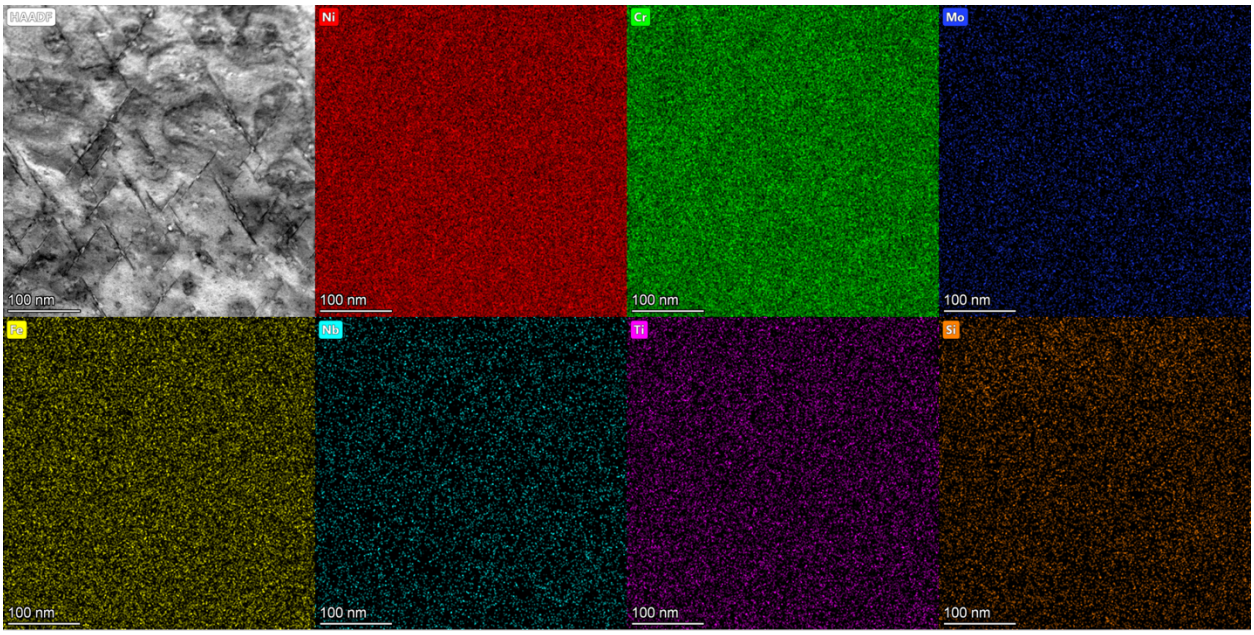

Figure 5: TEM EDS mapping of relevant chemical species showing no chemical segregation to the martensites or bubbles.

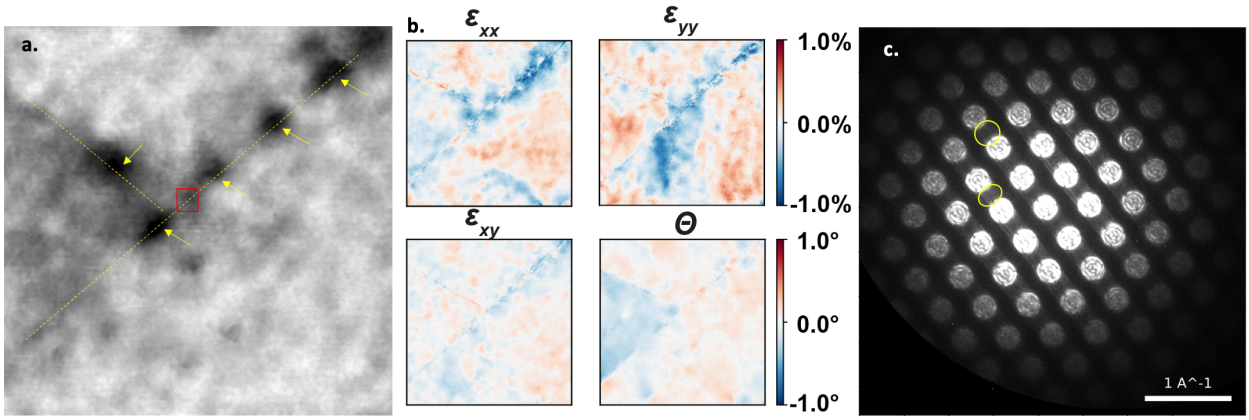

Figure 6. 4D STEM strain mapping of He implanted Alloy 625; (a) HAADF image with He bubbles arrowed and two intersecting planar martensite features marked by dashed lines; (b) corresponding strain maps showing principal x and y strains (ε_{xx}, ε_{yy}), shear (ε_{xy}) strain, and grain rotation (Θ), with blue indicating compression of atomic planes and red indicating tension of atomic planes in the strain maps; (c) diffraction pattern of red boxed area marked in (a) with streaks along {111} direction on [110] zone, several circled for ease of identification.

REFERENCES

1. M. J. Tadjer, J. L. Lyons, N. Nepal, J. A. Freitas, A. D. Koehler, and G. M. Foster, ECS Journal of Solid State Science and Technology **8**, Q3187 (2019).
2. A. Das and D. Basak, ACS Appl Electron Mater **3**, 3693 (2021).
3. M. Kaur, S. Gautam, and N. Goyal, Mater Lett **309**, 131356 (2022).
4. S.-M. Ma, T.-X. Wang, Z.-Y. Deng, X.-S. Zheng, B.-B. Wang, and H.-J. Feng, Phys Lett A **451**, 128400 (2022).
5. Y. Wang, X. Cheng, K. Zhang, G. Chen, R. Wang, and J. Zhang, Mater Adv **3**, 7384 (2022).
6. J. P. Wharry, H. (Claire) Xiong, T. Olsen, and C. Yang, in *Encyclopedia of Energy Storage* (Elsevier, 2022), pp. 243–255.
7. M. M. Rahman, W.-Y. Chen, L. Mu, Z. Xu, Z. Xiao, M. Li, X.-M. Bai, and F. Lin, Nat Commun **11**, 4548 (2020).
8. D. Garoli, L. V. Rodriguez De Marcos, J. I. Larruquert, A. J. Corso, R. Proietti Zaccaria, and M. G. Pelizzo, Applied Sciences **10**, 7538 (2020).
9. S. Peracchi, B. James, F. Pagani, V. Pan, J. Vohradsky, D. Bolst, D. A. Prokopovich, S. Guatelli, M. Petasecca, M. L. F. Lerch, S. H. Lee, T. Inaniwa, N. Matsufuji, M. Povoli, A. Kok, M. Jackson, T. Squire, A. B. Rosenfeld, and L. T. Tran, IEEE Trans Nucl Sci **68**, 897 (2021).
10. H. Huang, X. Yuan, L. Ma, J. Lin, G. Zhang, and B. Cai, Nuclear Engineering and Technology **55**, 2298 (2023).
11. M. Naito, S. Kodaira, R. Ogawara, K. Tobita, Y. Someya, T. Kusumoto, H. Kusano, H. Kitamura, M. Koike, Y. Uchihori, M. Yamanaka, R. Mikoshiba, T. Endo, N. Kiyono, Y. Hagiwara, H. Kodama, S. Matsuo, Y. Takami, T. Sato, and S. Orimo, Life Sci Space Res (Amst) **26**, 69 (2020).
12. S. Taller, G. VanCoevering, B. D. Wirth, and G. S. Was, Sci Rep **11**, 2949 (2021).
13. R. W. Harrison, Vacuum **160**, 355 (2019).
14. D. Rafaja, W. Valvoda, A. J. Perry, and J. R. Treglio, Surf Coat Technol **92**, 135 (1997).
15. T. Wohlenberg and W. A. Grantt, Phase Transitions **1**, 23 (1979).
16. C. A. Volkert, MRS Proceedings **157**, (1989).
17. G. W. Arnold, G. B. Krefft, and C. B. Norris, Appl Phys Lett **25**, 540 (1974).
18. T. Hioki, A. Itoh, S. Noda, H. Doi, J.-I. Kawamoto, and O. Kamigaito, Nuclear Instruments and Methods in Physics Research B **39**, 657 (1989).
19. D. Manova, G. Thorwarth, S. Mändl, H. Neumann, B. Stritzker, and B. Rauschenbach, Nucl Instrum Methods Phys Res B **242**, 285 (2006).
20. C. Blawert, B. L. Mordike, Y. Jirásková, and O. Schneeweiss, Surf Coat Technol **116–119**, 189 (1999).
21. S. Mandl and B. Rauschenbach, J Appl Phys **91**, 9737 (2002).
22. T. Hioki, A. Itoh, M. Ohkubo, S. Noda, H. Doi, J. Kawamoto, and O. Kamigaito, J Mater Sci **21**, 1321 (1986).
23. W. Primak and E. Monahan, J Appl Phys **54**, 435 (1983).
24. A. Benyagoub and S. Klaumünzer, Radiation Effects and Defects in Solids **126**, 105 (1993).
25. S. Klaumünzer, Radiation Effects and Defects in Solids **110**, 79 (1989).

26. A. Benyagoub, S. Löffler, M. Rammensee, S. Klaumünzer, and G. Saemann-Ischenko, Nucl Instrum Methods Phys Res B **65**, 228 (1992).
27. T. van Dillen, M. J. A. de Dood, J. J. Penninkhof, A. Polman, S. Roorda, and A. M. Vredenberg, Appl Phys Lett **84**, 3591 (2004).
28. C. Yang, T. Olsen, M. L. Lau, K. A. Smith, K. Hattar, A. Sen, Y. Wu, D. Hou, B. Narayanan, M. Long, J. P. Wharry, and H. Xiong, J Mater Res **37**, 1144 (2022).
29. W. J. Arora, H. I. Smith, and G. Barbastathis, Microelectron Eng **84**, 1454 (2007).
30. B. D. Chalifoux, Y. Yao, K. B. Woller, R. K. Heilmann, and M. L. Schattenburg, Opt Express **27**, 11182 (2019).
31. T. G. Bifano, H. T. Johnson, P. Bierden, and R. K. Mali, Journal of Microelectromechanical Systems **11**, 592 (2002).
32. T. Motooka and O. W. Holland, Appl Phys Lett **58**, 2360 (1991).
33. C. Koroni, T. Olsen, J. P. Wharry, and H. Xiong, Materials **15**, 5924 (2022).
34. Y. P. Sharkeev, A. N. Didenko, and E. V Kozlov, Surf Coat Technol **65**, 112 (1994).
35. Y. P. Sharkeev, E. V Kozlov, A. N. Didenko, S. N. Kolupaeva, and N. A. Vihor, Surf Coat Technol **83**, 15 (1996).
36. Y. P. Sharkeev, B. P. Gritsenko, S. V. Fortuna, and A. J. Perry, in *International Conference on Ion Implantation Technology, IEEE* (The Institute of Electrical and Electronics Engineers, Inc, 1998), pp. 873–876.
37. Y. P. Sharkeev and E. V Kozlov, Surf Coat Technol **158–159**, 219 (2002).
38. A. Misra, S. Fayeulle, H. Kung, T. E. Mitchell, and M. Nastasi, Nuclear Instruments and Methods in Physics Research B **148**, 211 (1999).
39. A. Misra, S. Fayeulle, H. Kung, T. E. Mitchell, and M. Nastasi, Appl Phys Lett **73**, 891 (1998).
40. D. J. Bacon, A. F. Calder, and F. Gao, Radiation Effects and Defects in Solids **141**, 283 (1997).
41. K. Dahmen, M. Giesen, J. Ikonomov, K. Starbova, and H. Ibach, Thin Solid Films **428**, 6 (2003).
42. P. H. Warren, C. D. Clement, C. Yang, A. Sen, W.-Y. Chen, Y. Wu, L. Wang, and J. P. Wharry, Journal of Nuclear Materials **583**, 154531 (2023).
43. C. Clement, Y. Zhao, P. Warren, X. Liu, S. Xue, D. W. Gandy, and J. P. Wharry, Journal of Nuclear Materials **558**, 153390 (2022).
44. D. P. Guillen, J. P. Wharry, G. Housley, C. D. Hale, J. Brookman, and D. W. Gandy, Nuclear Engineering and Design **402**, 112114 (2023).
45. J. P. Wharry, C. D. Clement, Y. Zhao, K. Baird, D. Frazer, J. Burns, Y. Lu, Y. Q. Wu, C. Knight, D. P. Guillen, and D. W. Gandy, Data Brief **48**, 109092 (2023).
46. C. Clement, S. Panuganti, P. H. Warren, Y. Zhao, Y. Lu, K. Wheeler, D. Frazer, D. P. Guillen, D. W. Gandy, and J. P. Wharry, Materials Science and Engineering: A **857**, 144058 (2022).
47. D. P. Guillen, D. C. Pagan, E. M. Getto, and J. P. Wharry, Materials Science & Engineering A **738**, 380 (2018).
48. J. F. Ziegler, (2013).
49. R. E. Stoller, M. B. Toloczko, G. S. Was, A. G. Certain, S. Dwaraknath, and F. A. Garner, Nucl Instrum Methods Phys Res B **310**, 75 (2013).
50. S. Han, L. Zhao, Q. Jiang, and J. Lian, Sci Rep **2**, 1 (2012).
51. B. H. Savitzky, S. E. Zeltmann, L. A. Hughes, H. G. Brown, S. Zhao, P. M. Pelz, T. C. Pekin, E. S. Barnard, J. Donohue, L. Rangel DaCosta, E. Kennedy, Y. Xie, M. T. Janish, M. M. Schneider, P.

Herring, C. Gopal, A. Anapolsky, R. Dhall, K. C. Bustillo, P. Ercius, M. C. Scott, J. Ciston, A. M. Minor, and C. Ophus, Microscopy and Microanalysis **27**, 712 (2021).
52. C. D. Clement, C. Yang, and J. P. Wharry, SSRN Pre-Print (n.d.).
53. F. Walsh, M. Zhang, R. O. Ritchie, A. M. Minor, and M. Asta, Nat Mater **22**, 926 (2023).
54. L. He, T. Yao, K. Bawane, M. Jin, C. Jiang, X. Liu, W. Chen, J. M. Mann, D. H. Hurley, J. Gan, and M. Khafizov, Journal of the American Ceramic Society **105**, 5419 (2022).
55. F. Walsh, M. Zhang, R. O. Ritchie, A. M. Minor, and M. Asta, Nat Mater **22**, 926 (2023).
56. J. Wang, M. B. Toloczko, N. Bailey, F. A. Garner, J. Gigax, and L. Shao, Nuclear Instruments and Methods in Physics Research B **387**, 20 (2016).
57. I. Kuryliszyn-Kudelska, J. Z. Domagała, T. Wojtowicz, X. Liu, E. Łusakowska, W. Dobrowolski, and J. K. Furdyna, J Appl Phys **95**, 603 (2004).
58. C. W. Tucker and J. B. Sampson, Acta Metallurgica **2**, 433 (1954).
59. C. Liu, B. Mensching, K. Volz, and B. Rauschenbach, Appl Phys Lett **71**, 2313 (1997).
60. B. H. Sencer, G. S. Was, H. Yuya, Y. Isobe, M. Sagisaka, and F. A. Garner, Journal of Nuclear Materials **336**, 314 (2005).
61. I. M. Ghauri and N. Afzal, J Phys D Appl Phys **40**, 6044 (2007).
62. E. Snoeks, K. S. Boutros, and J. Barone, Appl Phys Lett **71**, 267 (1997).
63. Y. C. Ku, H. I. Smith, and I. Plotnik, Journal of Vacuum Science & Technology B: Microelectronics and Nanometer Structures **6**, 2174 (1988).
64. B. Window and G. L. Harding, Journal of Vacuum Science & Technology A: Vacuum, Surfaces, and Films **11**, 1447 (1993).
65. Q. Wang, K. Ozaki, H. Ishikawa, S. Nakano, and H. Ogiso, Nuclear Instruments and Methods in Physics Research B **242**, 88 (2006).
66. H. Zhu, J. Davis, and Z. Li, Nucl Instrum Methods Phys Res B **455**, 83 (2019).
67. E. Hasenhuetl, Z. Zhang, K. Yabuuchi, P. Song, and A. Kimura, Nucl Instrum Methods Phys Res B **397**, 11 (2017).
68. C. Lu, K. Jin, L. K. Béland, F. Zhang, T. Yang, L. Qiao, Y. Zhang, H. Bei, H. M. Christen, R. E. Stoller, and L. Wang, Sci Rep **6**, 19994 (2016).
69. E. Getto, Z. Jiao, A. M. Monterrosa, K. Sun, and G. S. Was, Journal of Nuclear Materials **462**, 458 (2015).
70. M. R. Castell, Phys Rev B Condens Matter Mater Phys **68**, 1 (2003).
71. K. S. Mao, C. Sun, C.-H. Shiau, K. H. Yano, P. D. Freyer, A. A. El-Azab, F. A. Garner, A. French, L. Shao, and J. P. Wharry, Scr Mater **178**, 1 (2020).
72. K. S. Mao, A. J. French, X. Liu, Y. Wu, L. A. Giannuzzi, C. Sun, M. Dubey, P. D. Freyer, J. K. Tatman, F. A. Garner, L. Shao, and J. P. Wharry, Mater Des **206**, 109764 (2021).
73. G. S. Was, *Fundamentals of Radiation Materials Science: Metals and Alloys*, 2nd ed. (Springer, New York, 2017).
74. W. Zhang, Y. Xiong, J. Wu, W. Cheng, C. Du, S. Jin, B. Sun, and T. Shen, Nuclear Fusion **62**, 126034 (2022).
75. X. Xiao and L. Yu, Nuclear Materials and Energy **22**, 100721 (2020).
76. G. S. WAS and G. S. Was, *Fundamentals of Radiation Materials Science* (2017).
77. A. Debelle and A. Declémy, Nucl Instrum Methods Phys Res B **268**, 1460 (2010).
78. E. A. Clark, R. Yeske, and H. K. Birnbaum, Metallurgical Transactions A **11**, (1980).

79. K. S. Mao, C. Sun, X. Liu, H. J. Qu, A. J. French, P. D. Freyer, F. A. Garner, L. Shao, and J. P. Wharry, Journal of Nuclear Materials **528**, 151878 (2020).
80. K. S. Mao, C. Sun, Y. Huang, C.-H. Shiau, F. A. Garner, P. D. Freyer, and J. P. Wharry, Materialia (Oxf) **5**, 100208 (2019).
81. J. P. Wharry and K. S. Mao, J Mater Res **35**, 1660 (2020).
82. T. Masumura, K. Fujino, T. Tsuchiyama, S. Takaki, and K. Kimura, ISIJ International **61**, 546 (2021).
83. C. Yang, Y. Pachaury, A. El-Azab, and J. Wharry, Scr Mater **209**, 114394 (2022).
84. P. Hosemann, M. Sebastiani, M. Z. Mughal, X. Huang, A. Scott, and M. Balooch, J Mater Res **36**, 2349 (2021).
85. N. W. Phillips, H. Yu, S. Das, D. Yang, K. Mizohata, W. Liu, R. Xu, R. J. Harder, and F. Hofmann, Acta Mater **195**, 219 (2020).
86. C. Heintze, F. Bergner, and M. Hernández-Mayoral, Journal of Nuclear Materials **417**, 980 (2011).
87. M. Saleh, A. Xu, C. Hurt, M. Ionescu, J. Daniels, P. Munroe, L. Edwards, and D. Bhattacharyya, Int J Plast **112**, 242 (2019).
88. T. Miura, K. Fujii, K. Fukuya, and K. Takashima, Journal of Nuclear Materials **417**, 984 (2011).
89. S. Li, Y. Wang, X. Dai, F. Liu, J. Li, and X. Wang, Journal of Nuclear Materials **478**, 50 (2016).
90. T. Miyazawa, T. Nagasaka, R. Kasada, Y. Hishinuma, T. Muroga, H. Watanabe, T. Yamamoto, S. Nogami, and M. Hatakeyama, Journal of Nuclear Materials **455**, 440 (2014).
91. P. Hosemann, C. Vieh, R. R. Greco, S. Kabra, J. A. Valdez, M. J. Cappiello, and S. A. Maloy, Journal of Nuclear Materials **389**, 239 (2009).
92. C. D. Hardie, S. G. Roberts, and A. J. Bushby, Journal of Nuclear Materials **462**, 391 (2014).
93. C. Heintze, F. Bergner, S. Akhmadaliev, and E. Altstadt, Journal of Nuclear Materials **472**, 1 (2015).
94. R. Kasada, S. Konishi, K. Yabuuchi, S. Nogami, M. Ando, D. Hamaguchi, and H. Tanigawa, Fusion Engineering and Design **89**, 1637 (2014).
95. Y. Takayama, R. Kasada, Y. Sakamoto, K. Yabuuchi, A. Kimura, M. Ando, and D. Hamaguchi, **442**, 23 (2013).
96. A. Reichardt, A. Lupinacci, D. Frazer, N. Bailey, H. Vo, C. Howard, Z. Jiao, A. M. Minor, P. Chou, and P. Hosemann, Journal of Nuclear Materials **486**, 323 (2017).
97. H. Vo, A. Reichardt, C. Howard, M. D. Abad, D. Kaoumi, P. Chou, and P. Hosemann, Jom **67**, 2959 (2015).
98. T. Ajantiwalay, H. Vo, R. Finkelstein, P. Hosemann, and A. Aitkaliyeva, JOM (2019).
99. Y. Pachaury, G. Warren, J. P. Wharry, and A. El-Azab, International Journal of Plasticity, Submitted (n.d.).
100. A. Barnoush, P. Hosemann, J. Molina-Aldareguia, and J. M. Wheeler, MRS Bull **44**, 471 (2019).
101. N. Bibhanshu, M. N. Gussev, C. P. Massey, and K. G. Field, Materials Science and Engineering: A **832**, 142373 (2022).
102. M. A. Haque and M. T. A. Saif, Exp Mech **42**, 123 (2002).
103. D. Kiener, C. Motz, G. Dehm, and R. Pippan, International Journal of Materials Research **100**, 1074 (2009).

104. K. H. Yano, M. J. Swenson, Y. Wu, and J. P. Wharry, Journal of Nuclear Materials **483**, 107 (2017).
105. K. H. Yano, Y. Q. Wu, and J. P. Wharry, JOM **72**, 2065 (2020).
106. H. J. Qu, K. H. Yano, P. V. Patki, M. J. Swenson, and J. P. Wharry, J Mater Res **35**, 1037 (2020).
107. J. P. Wharry and K. H. Yano, Microscopy and Microanalysis **23**, 738 (2017).
108. P. H. Warren, G. Warren, M. Dubey, J. Burns, Y. Q. Wu, and J. P. Wharry, JOM **72**, 2057 (2020).
109. D. C. Bufford, C. M. Barr, B. Wang, K. Hattar, and A. Haque, JOM **71**, 3350 (2019).
110. C. Chisholm, Quantitative In Situ TEM Studies of Small-Scale Plasticity in Irradiated and Unirradiated Metals, University of California, Berkeley, 2015.
111. G. S. Jawaharram, P. M. Price, C. M. Barr, K. Hattar, R. S. Averback, and S. J. Dillon, Scr Mater **148**, 1 (2018).
112. D. Kiener, P. Hosemann, S. A. Maloy, and A. M. Minor, Nat Mater **10**, 608 (2011).
113. C. Robertson, B. K. K. Panigrahi, S. Balaji, S. Kataria, Y. Serruys, M.-H. H. Mathon, and C. S. S. Sundar, Journal of Nuclear Materials **426**, 240 (2012).
114. D. Kramer, H. Huang, M. Kriese, J. Robach, J. Nelson, A. Wright, D. Bahr, and W. W. Gerberich, Acta Mater **47**, 333 (1998).
115. S. H. Chen, L. Liu, and T. C. Wang, Int J Solids Struct **44**, 4492 (2007).
116. C. K. Dolph, D. J. da Silva, M. J. Swenson, and J. P. Wharry, Journal of Nuclear Materials **481**, 33 (2016).